RSC Advances

PAPER

View Article Online
View Journal | View Issue

Cite this: *RSC Adv.*, 2026, **16**, 7564

The effect of PVP coating on structural, optical, dielectric, and magnetic properties of an Fe_2O_3 nanostructure material for device engineering

Sayyed Wisal Ahmad,[a] Alamgir Khan,[a] Maryam Kamal,[a] Salhah Hamed Alrefaee,[b] Farkhod Rakhmonov,[c] Naseem Akhter,[d] Asad Ali, *[e] Vineet Tirth,[fg] Ali Algahtani[fh] and Abid Zaman *[i]

The impact of polyvinylpyrrolidone (PVP) coating compositions (2gm, 4gm, and 6gm) on the phase, magnetic, and dielectric characteristics of an Fe_2O_3 nanostructured material synthesized by the co-precipitation method are demonstrated in this experimental work. Structural analysis confirms the formation of hematite with a rhombohedral crystal structure and a rod-like morphology. According to spectroscopic techniques, the blue shift in absorption signifies the existence of vacancies and efficient PVP adherence to the nanostructure surfaces. Photoluminescence (PL) spectroscopy was employed to analyze the synthesized samples and identify the presence of different vacancies. Fourier transform infrared spectroscopy (FTIR) investigation has confirmed the stretching vibration mode of Fe–O. However, the thermogravimetric analysis (TGA) demonstrated the thermal stability of iron oxide. Dielectric measurements revealed strong frequency-dependent behaviors, with tangent loss and relative permittivity decreasing with increasing frequency. Additionally, different PVP coating compositions have a significant impact on magnetic properties, with coercivity decreasing and remanence increasing with high PVP concentration. Because of the diluting effect of the nonmagnetic polymer, the 2g PVP Fe_2O_3 sample with a thicker coating has various saturation magnetizations. These results showed that PVP content is a crucial factor in adjusting the magnetic and dielectric properties of a hematite nanostructure material.

Received 23rd December 2025
Accepted 26th January 2026

DOI: 10.1039/d5ra09948j

rsc.li/rsc-advances

1. Introduction

Nanostructure materials (NMs) are of great interest to many researchers because of their physical properties in comparison to bulk materials; in fact, they are simple to work with using various tools. Many nanoparticles (NPs), such as SiC/Fe_2O_3, $ZnCoFe_2O_4$/$CoFe_2O_4$, TiN/SiO_2, LiF, MnO_2/SiC Al_2O_3/Ag and ZrO_2/Ag are employed as filler material compounds in a range of polymeric matrices to modify the optical parameters for applications in optics and nano electronics by improving their structural, optical, magnetic and dielectric properties.[1–5] For instance, iron (Fe) NPs show great potential for usage in a variety of applications, such as drug delivery, cell labeling, MRI contrast agents, and therapies for hyperthermia. Fe_2O_3 NPs are the most widely used and favored iron oxide because of their stability, non-toxicity, biocompatibility, environmental friendliness, low manufacturing cost, and remarkable corrosion resistance. Furthermore, Fe_2O_3 NPs have high surface energies due to their large surface area-to-volume ratio (SAVR). Physiochemical properties and utilization of NPs are improved by reinforcing them into polymer matrices, which is beneficial for a variety of applications.[6–9] Fe_2O_3 NPs are a good example of inexpensive and non-toxic semiconductors, with a 2.2 eV bandgap energy, that can absorb a significant portion of the solar radiation, making them suitable for multiple applications like sensors, catalysis, the identification of cancer cells, and target drug delivery. In the colloidal phase, they are also important to modern technology like liquid sealing, charge transport, and magnetic storage systems devices.[10–13] To create a more stable state of NPs, the dipole–dipole interaction is adopted by triggering high surface energy. To overcome such challenges, surfactants, magnetic NPs, or polymers are used. Structural, microstructural,

[a]*Department of Physics, Abdul Wali Khan University Mardan, KP, 23200, Pakistan*
[b]*Department of Chemistry, College of Science, Taibah University Yanbu Governorate, Saudi Arabia*
[c]*School of Exact Sciences, National Pedagogical University of Uzbekistan named after Nizami, Uzbekistan*
[d]*Department of Physics, College of Science, Qassim University, Buraydah-51452, Saudi Arabia*
[e]*Department of Physics, Government Postgraduate College Nowshera, KP, 24100, Pakistan. E-mail: kasadiiui@gmail.com*
[f]*Mechanical Engineering Department, College of Engineering, King Khalid University, Abha 61421, Aseer, Kingdom of Saudi Arabia*
[g]*Centre for Engineering and Technology Innovations, King Khalid University, Abha 61421, Aseer, Kingdom of Saudi Arabia*
[h]*Research Center for Advanced Materials Science (RCAMS), King Khalid University, Guraiger, P.O. Box 9004, Abha-61413, Aseer, Kingdom of Saudi Arabia*
[i]*Department of Physics, Riphah International University, Islamabad 44000, Pakistan. E-mail: zaman.abid87@gmail.com*

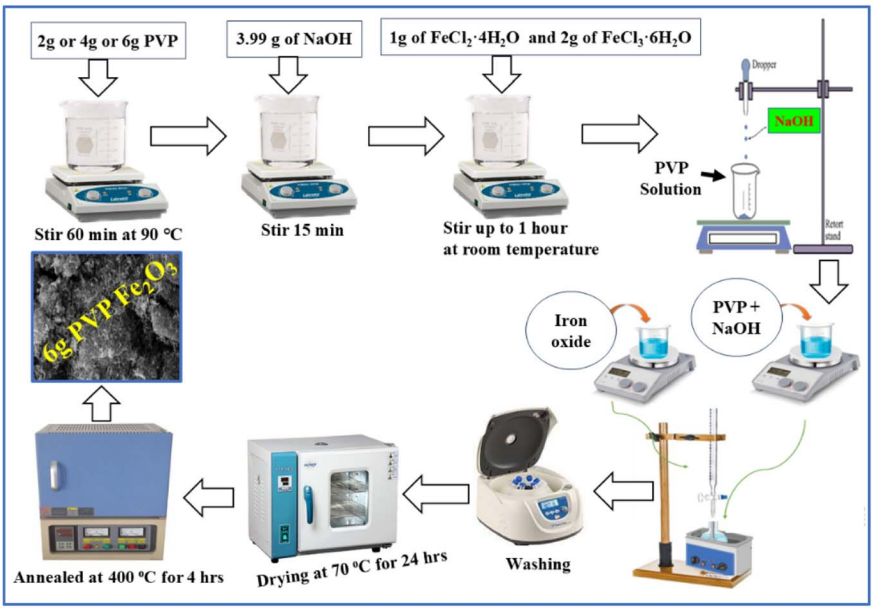

Fig. 1 Synthesis of pure and 2g, 4g, and 6g PVP, coated Fe_2O_3 nanostructures by co-precipitation method.

magnetic, optical, and dielectric properties of ferrites are strongly affected by wide bandgape, and synthesis process.[14–16] When ferrites are made through a ceramic approach, relatively irregular and large-sized particles are produced, which ultimately result in cavities and low densities. In order to overcome these challenges, wet chemical routes such as citrate gel, hydrothermal processing, co-precipitation, and combustion methods have been used to grow homogenous and ultra-fine-grained ferrites.[17–20] Polyvinylpyrrolidone (PVP) is a good method to significantly improve the functional properties of Fe_2O_3 NPs, particularly their magnetic and dielectric properties. PVP acts as a stabilizing agent, and flexible capping directly affects the material basic properties. It controls the growth and aggregation of particles, producing finer and more uniform nanoparticle sizes effectively.[21–24] The SEM results in a more homogeneous surface interface and fewer structural defects. Regarding dielectric and magnetic properties, the PVP shell's insulating qualities increased the dielectric constant and decreased tangent losses by preventing charge leakage and the interfacial polarization process at grain boundaries.[25,26] The reduction of surface spin disorder and suppression of particle agglomerations as common issues in nanoscale magnetic and dielectric material simultaneously improve saturation magnetization and coercivity in the magnetic domains. PVP alters the synthesis procedure to produce Fe_2O_3 nanoparticles with enhanced and customized electromagnetic performance for cutting-edge technological applications.[27–30] The current work investigates the variations in the structural, dielectric and magnetic properties of hematite PVP nanoparticles produced using the co-precipitation method.

2. Materials and method

The raw materials used in this experimental research work were purchased from Sigma-Aldrich Chemical Company. Hematite nanostructure samples are synthesized by first dissolving varying amounts of PVP (2, 4, and 6g) in 100 ml of water at 90 °C for 1 hour. Separately, 3.99 g of NaOH was dissolved in 100 ml of deionized water and an iron precursor solution was prepared by dissolving 1 g of $FeCl_2 \cdot 4H_2O$ and 2 g of $FeCl_3 \cdot 6H_2O$ in 25 ml of deionized water. The PVP solution was added dropwise to the NaOH solution, followed by the dropwise addition of the iron solution, with each step involving 10 min of agitation. The resulting precipitate was washed through centrifugation with deionized water and ethanol, dried at 70 °C for 24 hours and finally annealed at 400 °C for 4 hours, as shown in Fig. 1. For structural analysis X-rays diffraction (XRD, Bruker D8 Advance, Germany) with Cu-Kα radiation (λ = 1.5406 Å). The surface morphology and microstructural features were examined by using scanning electron microscopy (SEM, JEOL JSM-6490LV, Japan). Functional group identification was carried out by using Fourier transform infrared spectroscopy (FTIR, PerkinElmer Spectrum Two, USA) in the wavenumber range of 400–4000 cm^{-1}. The optical absorption measurements were performed by using a UV-Vis spectrophotometer (Shimadzu UV-2600, Japan) to find the optical bandgap energy. Dielectric properties were measured by using an impedance analyzer (Agilent E4991A, USA) over the selected frequency range. Magnetic measurements were carried out by using a vibrating sample magnetometer (VSM, Lakeshore 7407, USA) under an applied magnetic field at room temperature.

3. Results and discussion

3.1. X-ray analysis

X-ray diffraction (XRD) technique was used to investigate the phase purity and crystallinity of the synthesized samples. It is confirmed from XRD data that the samples is pure and coated crystalline in a rhombohedral structure by scanning at the

range of 20° to 70°. The XRD pattern is in good agreement with standard JCPDS card no. (00-011-1053), as shown in the Fig. 2. Table 1 shows average crystallite size (D), dislocation density (δ), and lattice strain (η) of Pure and PVP-coated (2g, 4g, 6g) Fe_2O_3 nanostructure, which could be calculated by using the given eqn (1)–(3) respectively.[31,32] We have calculated the error bars (assuming ±1%) instrumental uncertainty, which is standard for XRD-derived parameters *i.e.* crystallite size, dislocation density, and lattice strain.

$$D = \frac{0.9\lambda}{\beta \cos \theta} \quad (1)$$

In this case, 'β' represents 'Full Width at Half Maximum' (FWHM), 'θ' is the Bragg's peak angular location in radians, $k = 0.9$ and 'λ' is the wavelength (1.54 Å) of Cu-Kα radiation.

$$\delta = \frac{1}{D^2} \quad (2)$$

$$\eta = \frac{\beta \cos \theta}{4} \quad (3)$$

The absence of any extra peak corresponding to impurity phase confirms the high purity Fe_2O_3 NPs and lack of secondary phase formations.[33,34] A slight phase shift in the diffraction peaks is observed for the PVP-coated sample, which is attributed to the variation in lattice parameters resulting from the successful incorporation of PVP into Fe_2O_3 NPs. The average crystalline sizes were calculated using Shere eqn (1); for pure Fe_2O_3 the crystallized size is 24.9 nm, while the sizes for coated samples (2, 4, and 6g) were 20, 20.2, and 20.4 nm, respectively. These results indicate that the crystallite size increases slightly with higher PVP concentration yet remains smaller than that of the pure Fe_2O_3.[35,36]

3.2. FE-SEM and EDS studies

Fig. 3(a–h) shows the FE-SEM images of the synthesized samples, which were used to evaluate their surface morphology,

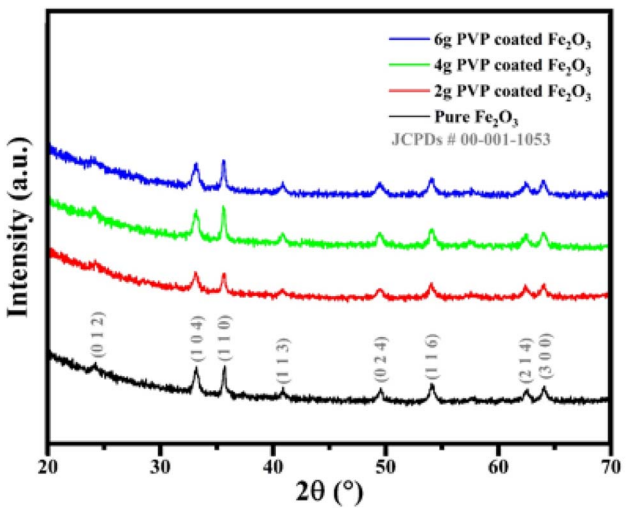

Fig. 2 XRD pattern of pure-Fe_2O_3 and PVP-coated (2g, 4g, 6g) Fe_2O_3.

Table 1 Physical properties of pure-Fe_2O_3 and PVP-coated (2g, 4g, 6g) Fe_2O_3

Composition	D (nm)	δ ($\times 10^{-5}$ nm^{-2})	η ($\times 10^{-3}$)
Pure Fe_2O_3	347.69 ± 3.4	0.8272 ± 0.01	0.9969 ± 0.01
2g PVP coated Fe_2O_3	276.32 ± 2.7	1.3097 ± 0.02	1.2545 ± 0.02
4g PVP coated Fe_2O_3	135.18 ± 1.4	5.4726 ± 0.05	2.5643 ± 0.02
6g PVP coated Fe_2O_3	113.99 ± 1.1	7.6955 ± 0.07	3.0408 ± 0.03

homogeneity, and dispersion behavior within the polymer matrix. According to Fig. 3(a and b), the product sample is pure Fe_2O_3 exhibits noticeable agglomeration and relatively rough surfaces while Fig. 3(c and d) is PVP-coated samples show well-defined rhombohedral rod-like morphologies with significantly improved particle separation. As the PVP contents increased, the nanostructures retained their core shape while displaying smoother surfaces and a more even spatial distribution as shown in Fig. 3(e–h).[37] The elemental composition of the prepared samples was analyzed by using energy-dispersive X-ray spectroscopy (EDS). Fig. 4(a) shows the spectrum of pure Fe_2O_3 sample revealed that only Fe, and O peaks, confirmed the purity of the hematite phase while Fig. 4(b–d) shows the spectra of PVP coated samples exhibit additional C and N signals, originating from the polymer chains of PVP. The consistent presence of Fe, O, C, and N across the analyzed regions indicated a uniform polymer coating and homogeneous distribution of Fe_2O_3 within the PVP matrix. No impurity-related peaks were detected, further indorsing the chemical stability of the prepared samples.[38] Overall, the combined SEM and EDS analysis provides strong evidence that a PVP coating significantly improves the homogeneity and dispersion of Fe_2O_3 nanostructure.

3.3. UV spectrophotometry analysis

Optical absorption analysis revealed that all samples absorb radiation strongly in the UV-Vis, range as shown in Fig. 5(a), and reported the spectra is shifting slightly as PVP concentration increased. The optical band gap determined from Tauc plot as shown in Fig. 5(b), representing a clear blue shift widening from 1.32 eV for pure while 1.68, 1.57, and 1.43 eV for the coated samples (2gm, 4gm, and 6g PVP) respectively. This variation in bandgap energy is attributed to the changes in particle growth and agglomeration, polymer–particle interaction, leading to improved size uniformity and surface passivation due to PVP coating contents, consistent with previously reported polymer ferrites and polymer related nanoparticle systems.[39–42]

3.4. Fourier transform infrared (FTIR) spectroscopy analysis

FTIR spectroscopy was used to identify functional groups in the pure and PVP-coated samples in the range of 400–4500 cm^{-1} wavenumber as shown in Fig. 6. The Fe–O stretching vibrations are observed at 410 cm^{-1} and 516 cm^{-1}, while two minor peaks at 1355 cm^{-1} and 3455 cm^{-1} correspond to N–O and OH stretching modes respectively. In the PVP-coated samples, characteristic PVP bands appear at 1642 cm^{-1} (C=O stretching)

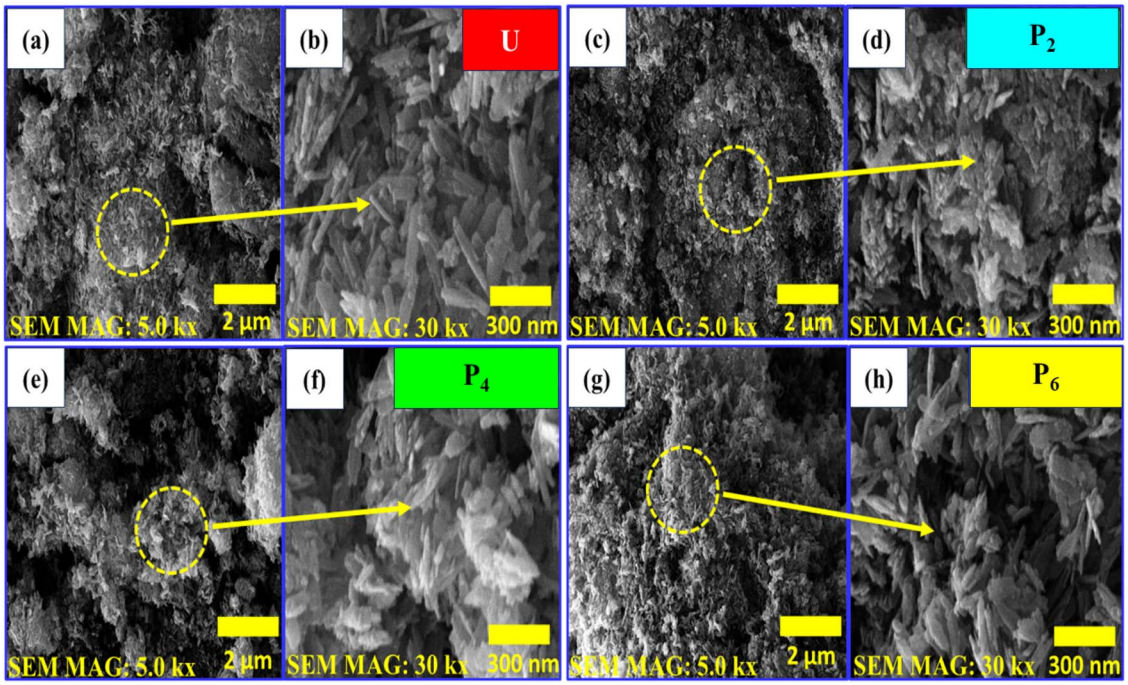

Fig. 3 FE-SEM images of (a) & (b) pure-Fe_2O_3, (c) & (d) 2g PVP coated (e) & (f) 4g PVP coated, and (g) & (h) 6g PVP coated.

and 1426 cm^{-1} (C–H bending).[43] Particularly, variations in the intensity of these absorption peaks indicated the extent of surface interaction between PVP and ferrite particles. Increased intensity of the C–H and C=O bands reflects stronger polymer–particle interactions, leading to enhanced surface passivation and reduced surface defects. This improved surface environment correlates with the observed modifications in optical properties, magnetic behavior (*e.g.*, reduced coercivity), and overall structural stability of the coated samples.[44]

3.5. Photoluminescence (PL) spectroscopy

PL spectroscopy is a valuable technique for analyzing the optical properties of semiconductor defects, helping to distinguish between intrinsic and extrinsic origins. The PL spectrum in

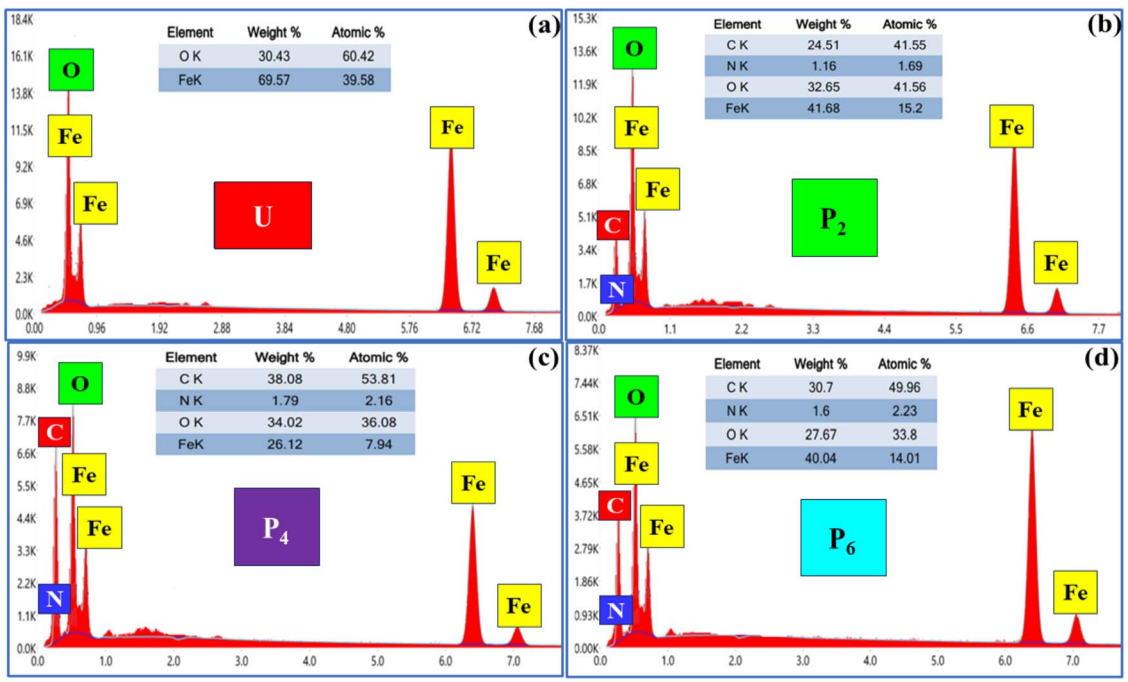

Fig. 4 EDS analysis of (a) pure-Fe_2O_3, (b) 2g PVP coated (c) 4g PVP coated, and (d) 6g PVP coated.

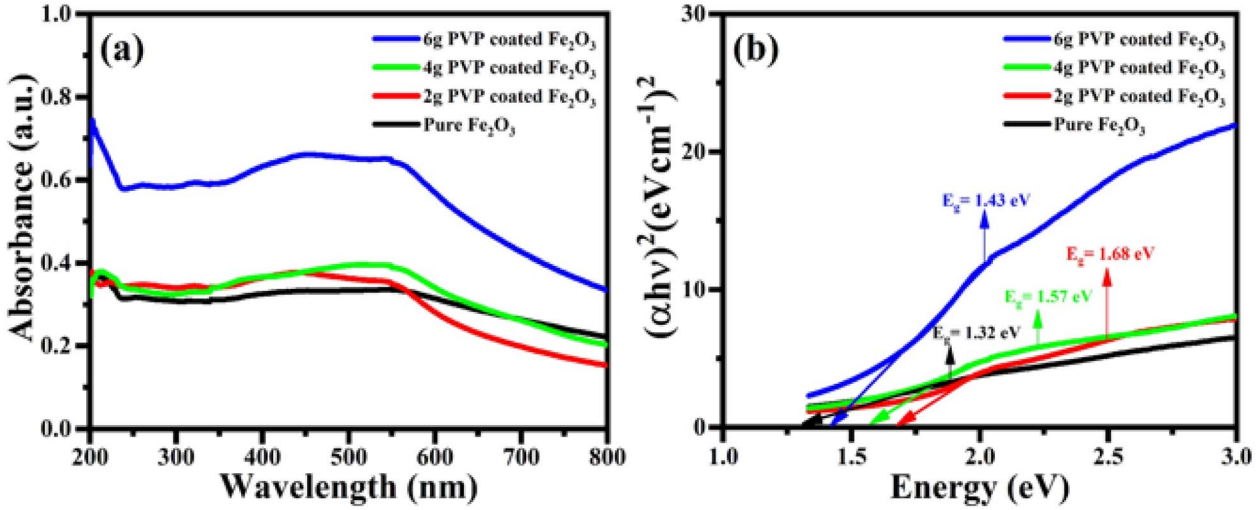

Fig. 5 UV-Vis, spectra of pure-Fe_2O_3 and PVP-coated (2g, 4g, 6g) Fe_2O_3 (a) absorption spectra and (b) band gap energy.

Fig. 7 of pure exhibits several peaks attributable to excitonic transitions. The violet emission at 442 nm arises from electron transition to the valence band. The series of red emissions (650, 678, 714, 734, and 765 nm) are primarily caused by electron transitions from various donor levels associated with oxygen vacancies to the valence band.[45] The intensity of PL emission spectra is correlated with defect concentration. The samples coated with 2g PVP show a more intense spectrum, indicating higher density vacancies than the samples coated with 4g and 6g of PVP, respectively, which exhibit small defects.[46] The findings or outcomes of the current research work are related to UV-visible absorption spectra as well as SEM investigations.

3.6. Thermo gravimetric analysis (TGA)

Fig. 8 shows the thermal stability of the materials varies significantly. Pure Fe_2O_3 NPs (black curve, U) show exceptional stability, keeping a constant mass across the temperature range. In contrast to pure PVP, the polymers are completely degraded by 450 °C temperature, while the thickness of the coating on the PVP-coated samples is directly regulating the level of protection. Thinner coating (red curve, P2) results in greater mass loss, while thicker coating (green P4 and blue P6) progressively enhances the thermal shielding, with the thicker coating (blue color) showing the minimum mass loss.[47] This reveals that a robust PVP layer slows degradation, protecting the Fe_2O_3 core, a critical insight for high-temperature applications in sensing, catalysis, and magnetism.

$$t = R[1 + (\rho cmv/\rho mcv)]1/3 - R \quad (4)$$

In eqn (4), '*mv*' and 'ρv' represented the density and mass of the prepared samples (ρv = 4.87 g cm^{-3} and mv = 0.654314 respectively), whereas '*R*' is the radius of the coated samples. The masses and densities of the coated samples are denoted by '*mc*' (0.741416, 0.730306, 0.54605) and 'ρc' (=1.67 g cm^{-3}). The values of the synthesized samples *i.e.* P2, P4, and P6 is 61%, 61.4%, and 50% respectively.

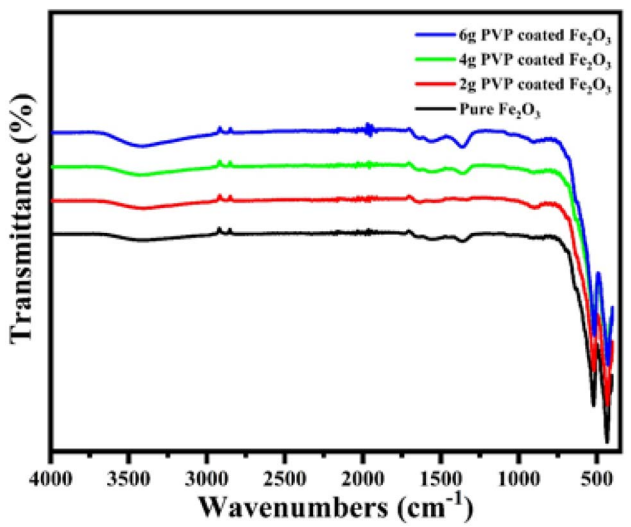

Fig. 6 FTIR spectra of pure-Fe_2O_3 and PVP-coated (2g, 4g, 6g) Fe_2O_3.

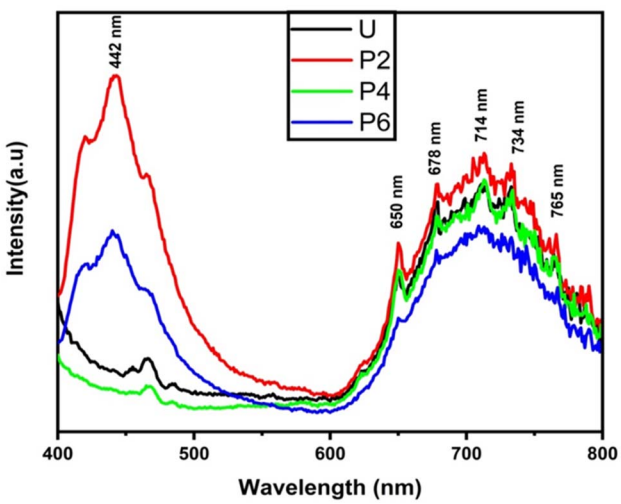

Fig. 7 PL spectra of pure-Fe_2O_3 and PVP-coated (2g, 4g, 6g) Fe_2O_3.

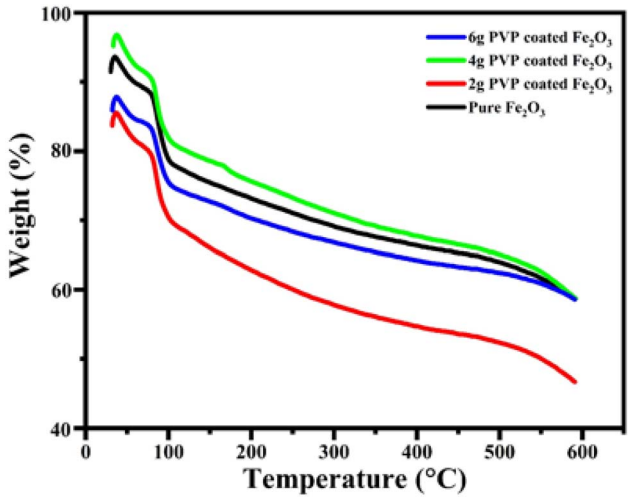

Fig. 8 TGA plots of pure-Fe_2O_3 and PVP-coated (2g, 4g, 6g) Fe_2O_3.

3.7. Dielectric properties

To obtain the dielectric properties, we had compressed the synthesized powder into circular pellets and annealed them at 600 °C for one hour by using a high energy furnace. Electrodes are fabricated by drying the pellets at 100 °C in an oven and applying silver paste to both sides, producing a parallel plate conductive surface. By using impedance analyzer spectroscopy, we have measured the dielectric constant or relative permittivity, as a function of frequency for both pure and coated PVP samples.[48] Eqn (5) is used to find the value of the complex relative permittivity (ε^*),

$$\varepsilon^* = \varepsilon' - j\varepsilon'' \quad (5)$$

ε' represented the real part known as dielectric constant and ε'' represents the imaginary part known as dielectric loss.

Fig. 9(a) shows the variation of dielectric constants (ε_r) with frequency. The 2g coated PVP sample exhibits the highest value of dielectric constant, while the 4g PVP, pure Fe_2O_3 NPs, and 6g PVP-coated samples follow in descending order.[49] The elevated value of the dielectric constant at low frequency is primarily due to the contribution of the rotational directional polarization and space charge polarization. The rotational directional polarization involves the alignment of dipoles with the applied electric field, while space charge polarization results from charge carriers being trapped at defective sites.[50] The superior performance of the 2g and 4g samples shows a higher concentration of such defects, which act as charge carrier traps. The electric field oscillates too quickly for this type of polarization mechanism, causing ε_r to diminish as frequency increases. The tangent loss (ε'') is calculated by using eqn (6),,[51]

$$\varepsilon'' = \varepsilon' \tan\delta \quad (6)$$

Fig. 9(b) shows the tangent loss for both pure and coated nanostructure samples. The plot reveals that tangent loss is higher at the low frequency, moderate at the intermediate

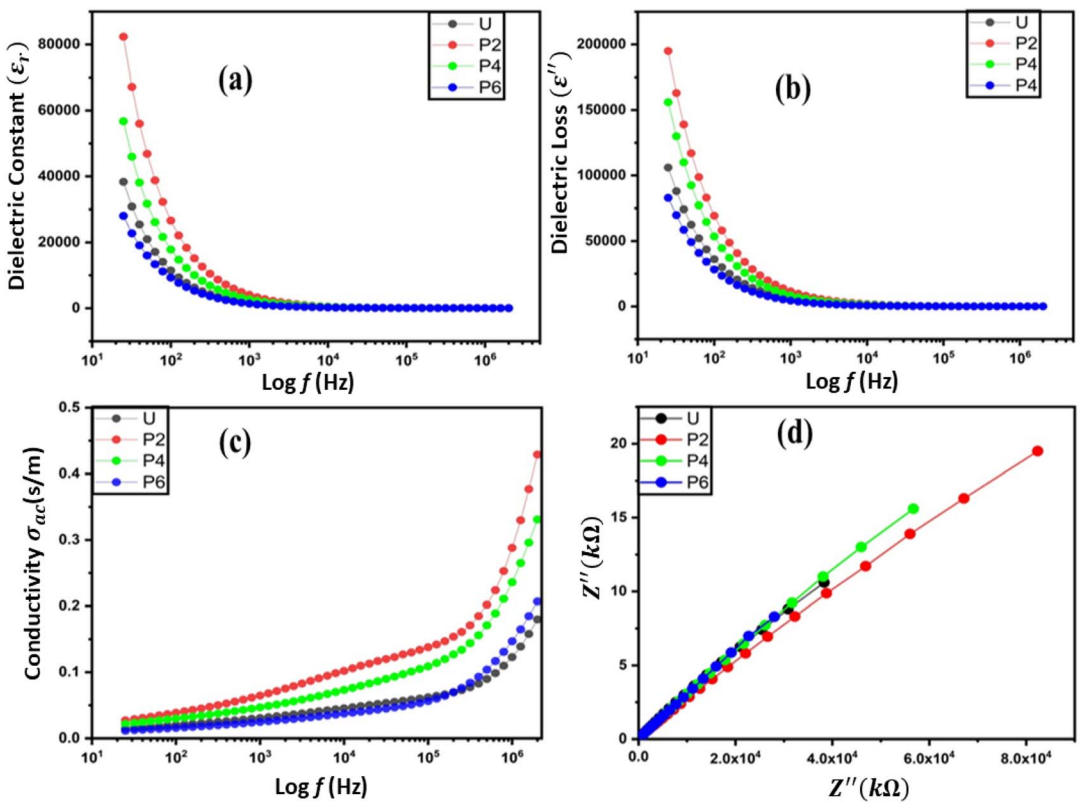

Fig. 9 Variation of pure-Fe_2O_3 and PVP-coated (2g, 4g, 6g) Fe_2O_3 (a) dielectric constant, (b) dielectric loss (c) conductivity and (d) Nyquist plot.

Table 2 Remanence, coercivity, and magnetization of the prepared samples

S. no.	Sample	Coercivity (A m^{-1})	Remanence (T)	Saturation magnetization (A m^{-1})
1	U	75.88 ± 0.76	0.01149 ± 0.0001	0.503 ± 0.005
2	P2	35.59 ± 0.36	0.00890 ± 0.0001	0.889 ± 0.009
3	P4	42.83 ± 0.43	0.01093 ± 0.0001	0.497 ± 0.005
4	P6	59.56 ± 0.60	0.01859 ± 0.0002	0.550 ± 0.006

frequency, and lowest at the higher frequency range. Among these samples, the P2 (2g coated) sample possesses the most significant tangent loss. It can be attributed to the misalignment of the dipoles with the applied electric field, causing energy dissipation in the form of heat rather than storage. Reduced dielectric loss at high frequencies is probably caused by restrictions on ion mobility, domain wall motion, and space charge polarization. Due to its lowest relative permittivity and tangent losses in the high-frequency region, it is suitable for high-frequency device applications.[52,53] Metallic ionic bonding seems to have an effect on tangent losses at low and intermediate frequencies. The overall tangent losses tendency across the samples *i.e.*, highest for the P2 (2g) coated sample, followed by the P4 (4g), U (pure), and P6 (6g) coated samples are correlated with the density defect observed in the EDS and PL investigations, where defect concentration increases with tangent losses. Fig. 9(c) shows the AC conductivity of both pure and coated samples. The AC conductivity is small at lower frequency and increases at mid frequency while rising sharply at the higher frequency region.[54,55] This behavior is attributed to suppress conduction and trapping of charge carriers at the lowest frequency region. As frequency increases, the charge carrier gains sufficient energy to be released from the traps, leading to a rapid improvement in AC conductivity.[56,57]

The ac conductivity will be calculated for all samples by using eqn (7).

$$\sigma_{ac} = \varepsilon_o \, \varepsilon' \tan \delta 2\pi f \quad (7)$$

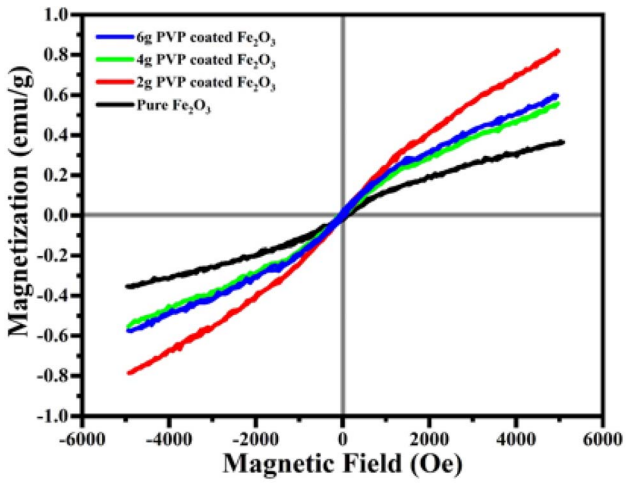

Fig. 10 Magnetic properties of pure-Fe_2O_3 and PVP-coated (2g, 4g, 6g) Fe_2O_3.

Analysis revealed a strong dependence on the PVP coating concentrations. The sample of 2g PVP coating possess the maximum values, while the 6g PVP coating sample shown the minimum values. Fig. 9(d) shows the Nyquist plot for visualizing the electrochemical impedance spectroscopy (EIS) data. The predominantly linear trend is observed for all samples are characterized by the absence of semi-circular arcs, indicated a dominated resistive system along with minimal capacitive contributions.[58,59] The sample P2 has the highest net resistance, suggesting has to charge transfer, likely due to its microstructural investigations.

3.8. Magnetic properties

Magnetic characteristic is the response of a material inside a magnetic field. The main property is coercivity, which is the resistance of material to being demagnetized. A material with high coercivity will retain its magnetization behaviors even when exposed to an external magnetic field.[60,61] Table 2 shows the significant impact of PVP coating on the magnetic properties of the pure as well as PVP-coated samples. The sample U has the 75.88 highest value of coercivity, which is due to the demagnetization process.[62] The coercivity, however, progressively decreases as the thickness of the PVP coating increases, following the sequence from P2 (35.59) to P4 (42.83) and then to P6 (59.56). When the external magnetic field is removed, the coercivity and remanence are correlated.[63,64]

In this regarded sample P6 exhibits the highest remanence (0.0186) values among PVP coating samples, suggesting a greater retained magnetic effect after exposure to a field. It is observed that sample *U* has high coercivity while having lower remanence (0.0115) than sample P6. When striking a strong magnetic field on a magnetic material, a saturation magnetization is obtained.[65] Here the sample P2 demonstrated the highest saturation magnetization (0.890), as visually confirmed in Fig. 10. A clear declination in saturation magnetization is reported for samples P4 and P6, indicating that the magnetic responsiveness is compromised with the thickness of coatings. From Table 2, these quantities are fully consistent with the magnetic properties observed in the hysteresis loop. The plot for sample P2 shows a steeper slope in the region approaching positive saturations, which is directly correlated with strong saturated magnetization. The overall slopes and shapes of these curves systematically vary with increasing PVP coating contents.

4. Conclusion

Pure Fe_2O_3 NPs and PVP-coated samples were prepared by using the co-precipitation technique. The XRD pattern confirmed the

formation of a single-phase rhombohedral wurtzite structure, with peak broadening associated with the small crystallite size of the nanostructure and the presence of the PVP coating. The average calculated crystallite sizes reduce from 25.2 nm to 20 nm due to coating concentration. SEM analysis revealed rod-like morphology, while FTIR and EDS spectra confirmed the functional groups and elemental compositions of the samples along with no extra peak. The PL and UV-Vis spectra show a tunable bandgap energy that increases from 1.32 eV to 1.68 eV, indicating a blue shift with the initial coating. EIS showed a characteristic decline in dielectric constant with increasing frequency, while AC conductivity was enhanced with higher PVP contents. The iron oxide core is thermally stable after PVP treatment and decomposes at 450 °C. Magnetically, the coating reduced the coercivity of the P2 (2g) sample, which showed the highest saturation magnetization. These findings confirm that PVP coating concentration as a key parameter for optimizing Fe_2O_3 nanostructures for sensor, data storage, and photocatalytic applications.

Conflicts of interest

The authors declare no conflicting of interest.

Data availability

The data will be made available on reasonable request.

Acknowledgements

The authors extend their appreciation to the Deanship of Research and Graduate Studies at King Khalid University, Kingdom of Saudi Arabia, for funding this work through the Large Research Group Project under the grant number RGP2/149/46.

References

1 S. C. Watawe, U. A. Bamne, S. P. Gonbare and R. B. Tangsali, Preparation and dielectric properties of cadmium substituted lithium ferrite using microwave-induced combustion, *Mater. Chem. Phys.*, 2007, **103**(2–3), 323–328.
2 H. F. Chen, X. Y. Tao, B. H. Zhu, J. T. Pan, L. L. Ma, C. Chen, W. G. Zhu, W. Chen and Y. Q. Lu, Reconfigurable nonlinear Pancharatnam-Berry diffractive optics with photopatterned ferroelectric nematics, *Light: Sci. Appl.*, 2025, **14**(1), 314.
3 M. Gunawan, M. Priest, D. Gunawan, S. Nie, A. Satriyatama, J. Vongsvivut, Z. Hameiri, Q. Zhang, S. Zhou and R. Amal, Differentiating the role of Ni and Fe in NiFeOx co-catalyzed BiVO4 photoanode for water oxidation, *Energy Environ. Sustainability*, 2025, **1**(2), 100019.
4 S. T. Abd El-Latif, K. M. Ahmed, S. I. Elkalashy and M. F. Zaki, Atmospheric–pressure DBD plasma modifying photoemission, optical and electrical properties of polycarbonate films, *Inorg. Chem. Commun.*, 2024, **161**, 112048.
5 S. Choudhary, Structural, optical, dielectric and electrical properties of (PEO–PVP)–ZnO nanocomposites, *J. Phys. Chem. Solids*, 2018, **121**, 196–209.
6 X. Wang, K. Maeda, A. Thomas, K. Takanabe, G. Xin, J. M. Carlsson, K. Domen and M. Antonietti, A metal-free polymeric photocatalyst for hydrogen production from water under visible light, *Nat. Mater.*, 2009, **8**(1), 76–80.
7 J. Brillet, M. Gratzel and K. Sivula, Decoupling feature size and functionality in solution-processed, porous hematite electrodes for solar water splitting, *Nano Lett.*, 2010, **10**(10), 4155–4160.
8 Y. Guan, Y. Ding, Y. Fang, J. Li, Y. Liu, R. Wang, J. Hao, H. Xie, C. Xu, L. Zhen and Y. Li, Far-field femtosecond laser-driven λ/73 super-resolution fabrication of 2D van der Waals NbOI2 nanostructures in ambient air, *Nat. Commun.*, 2025, **16**(1), 4149.
9 G. F. Goya, T. S. Berquo, F. C. Fonseca and M. P. Morales, Static and dynamic magnetic properties of spherical magnetite nanoparticles, *J. Appl. Phys.*, 2003, **94**(5), 3520–3528.
10 Y. Zhao, Co-precipitated Ni/Mn shell coated nano Cu-rich core structure: A phase-field study, *J. Mater. Res. Technol.*, 2022, **21**, 546–560.
11 J. Y. Lu, Z. Q. Bu, Y. Q. Lei, D. Wang, B. He, J. Wang and W. T. Huang, Facile microwave-assisted synthesis of Sb2O3-CuO nanocomposites for catalytic degradation of p-nitrophenol, *J. Mol. Liq.*, 2024, **409**, 125503.
12 A. M. Davarpanah, A. Rahdar, M. A. Dastnae, O. Zeybek and H. Beyzaei, (1-x) BaFe12O19/xCoFe2O4 hard/soft magnetic nanocomposites: synthesis, physical characterization, and antibacterial activities study, *J. Mol. Struct.*, 2019, **1175**, 445–449.
13 S. Wang, Z. Zhang, C. Sun, L. Gong, X. Zhang, S. Gao, C. Zhang, Q. Han and S. Yan, Multifunctional tribovoltaic coating for self-powered *in situ* sensing with exceptional tribological robustness and charge transport, *Adv. Funct. Mater.*, 2025, e14190.
14 M. Chastellain, A. Petri and H. Hofmann, Particle size investigations of a multistep synthesis of PVA coated superparamagnetic nanoparticles, *J. Colloid Interface Sci.*, 2004, **278**(2), 353–360.
15 A. D. Sheikh and V. L. Mathe, Anomalous electrical properties of nanocrystalline Ni–Zn ferrite, *J. Mater. Sci.*, 2008, **43**(6), 2018–2025.
16 P. P. Hankare, R. P. Patil, U. B. Sankpal, S. D. Jadhav, P. D. Lokhande, K. M. Jadhav and R. Sasikala, Investigation of structural and magnetic properties of nanocrystalline manganese substituted lithium ferrites, *J. Solid State Chem.*, 2009, **182**(12), 3217–3221.
17 J. Liang, F. Ye, Q. Song, Y. Cao, S. Hui, Y. Qin and H. Wu, In-Plane heterogeneous Structure-Boosted interfacial polarization in graphene for wide-band and wide-temperature microwave absorption, *Chem. Eng. J.*, 2024, **497**, 154307.
18 S. A. Ealia and M. P. Saravanakumar, A review on the classification, characterisation, synthesis of nanoparticles

and their application, *IOP Conf. Ser. Mater. Sci. Eng.*, 2017, **263**(3), 032019.

19 X. Lu, W. Zhang, C. Wang, T. C. Wen and Y. Wei, One-dimensional conducting polymer nanocomposites: Synthesis, properties and applications, *Prog. Polym. Sci.*, 2011, **36**(5), 671–712.

20 J. Ivorra-Martinez, I. Ferrer, R. Aguado, M. Delgado-Aguilar, M. L. Garcia-Romeu and T. Boronat, Development of P (3HB-co-3HHx) nanohydroxyapatite (nHA) composites for scaffolds manufacturing by means of fused deposition modeling, *Int. J. Bioprint.*, 2023, **10**(1), 0156.

21 Z. Wang, H. Lin, Y. Wang, X. Yin, J. Li and Y. Wang, Tribological Behavior of Zwitterionic-Polyester Composite Films with Phase-Separated Structures, *Langmuir*, 2025, **41**(45), 30167–30173.

22 L. Yuan, X. H. Lu, X. Xiao, T. Zhai, J. Dai, F. Zhang, B. Hu, X. Wang, L. Gong, J. Chen and C. Hu, Flexible solid-state supercapacitors based on carbon nanoparticles/MnO2 nanorods hybrid structure, *ACS Nano*, 2012, **6**(1), 656–661.

23 V. M. Ustinov, A. E. Zhukov, A. R. Kovsh, S. S. Mikhrin, N. A. Maleev, B. V. Volovik, Y. G. Musikhin, Y. M. Shernyakov, E. Y. Kondat'eva, M. V. Maximov and A. F. Tsatsul'nikov, Long-wavelength quantum dot lasers on GaAssubstrates, *Nanotechnology*, 2000, **11**(4), 397.

24 Z. Y. Zhao and Q. L. Liu, Study of the layer-dependent properties of MoS2 nanosheets with different crystal structures by DFT calculations, *Catal. Sci. Technol.*, 2018, **8**(7), 1867–1879.

25 L. Qiu, V. G. Pol, J. Calderon-Moreno and A. Gedanken, Synthesis of tin nanorods *via* a sonochemical method combined with a polyol process, *Ultrason. Sonochem.*, 2005, **12**(4), 243–247.

26 S. Mallakpour and H. Y. Nazari, The influence of bovine serum albumin-modified silica on the physicochemical properties of poly (vinyl alcohol) nanocomposites synthesized by ultrasonication technique, *Ultrason. Sonochem.*, 2018, **41**, 1–10.

27 N. A. Ramin, M. R. Ramachandran, N. M. Saleh, Z. M. Mat Ali and S. Asman, Magnetic nanoparticles molecularly imprinted polymers: a review, *Curr. Nanosci.*, 2023, **19**(3), 372–400.

28 Y. T. Jia, J. Gong, X. H. Gu, H. Y. Kim, J. Dong and X. Y. Shen, Fabrication and characterization of poly (vinyl alcohol)/chitosan blend nanofibers produced by electrospinning method, *Carbohydr. Polym.*, 2007, **67**(3), 403–409.

29 T. Zhang, H. Hu, H. Jiang, Z. Wang, J. Lin, Y. Cheng, W. Guo, D. Ke, H. Hang, M. Ta and J. Ou-Yang, KNN-based frequency-adjustable ferroelectric heterojunction and biomedical applications, *Nat. Commun.*, 2025, **16**(1), 7120.

30 K. Nagaveni, M. S. Hegde and G. Madras, Structure and photocatalytic activity of Ti1-x M x O2±δ (M= W, V, Ce, Zr, Fe, and Cu) synthesized by solution combustion method, *J. Phys. Chem. B*, 2004, **108**(52), 20204–20212.

31 A. Zaman, S. Uddin, N. Mehboob, A. Ali, A. Ahmad and K. Bashir, Effect of Zr4+ on the structural and microwave dielectric properties of CaTiO3 ceramics, *Ferroelectrics*, 2021, **577**(1), 143–152.

32 M. Abbas, R. Ullah, K. Ullah, F. Sultana, A. Mahmood, A. Mateen, Y. Zhang, A. Ali, K. Althubeiti, M. Mushtaq and A. Zaman, Structural, optical, electrical and dielectric properties of (Sr1-xMgx)(Sn0. 5Ti0. 5) O3 (X= 0.00, 0.25, 0.50, 0.75) ceramics *via* solid state route, *Ceram. Int.*, 2021, **47**(21), 30129–30136.

33 S. K. Durrani, S. Z. Hussain, K. Saeed, Y. Khan, M. Arif and N. Ahmed, Hydrothermal synthesis and characterization of nanosized transition metal chromite spinels, *Turk. J. Chem.*, 2012, **36**(1), 111–120.

34 Ö. Ece, *Hydrothermal synthesis and structural characterization of open-framework metal phosphates templated with organic diamines*, Izmir Institute of Technology, Turkey, 2012.

35 T. A. Elnsar, M. H. Soliman and M. A. Ayash, Modified hydroxyapatite adsorbent for removal of iron dissolved in water wells in Sohag, Egypt, *Chem. Adv. Mater.*, 2017, **1**(2), 1–3.

36 L. R. Khot, S. Sankaran, J. M. Maja, R. Ehsani and E. W. Schuster, Applications of nanomaterials in agricultural production and crop protection: a review, *Crop Prot.*, 2012, **35**, 64–70.

37 F. Cardarelli, *Materials Handbook: A Concise Desktop Reference*, London, Springer London, 2008.

38 K. R. Zulfiqar, M. U. Rahman and Z. Iqbal, Variation of structural, dielectric and magnetic properties of PVP coated γ-Fe2O3 nanoparticles, *J. Mater. Sci.: Mater. Electron.*, 2016, **27**(12), 12490–12498.

39 A. M. El Nahrawy, B. A. Hemdan, A. M. Mansour, A. Elzwawy and A. B. Abou Hammad, Integrated use of nickel cobalt aluminoferrite/Ni2+ nano-crystallites supported with SiO2 for optomagnetic and biomedical applications, *Mater. Sci. Eng., B*, 2021, **274**, 115491.

40 A. M. El Nahrawy, A. I. Ali, A. M. Mansour, A. B. Abou Hammad, B. A. Hemdan and S. Kamel, Talented Bi0. 5Na0. 25K0. 25TiO3/oxidized cellulose films for optoelectronic and bioburden of pathogenic microbes, *Carbohydr. Polym.*, 2022, **291**, 119656.

41 L. Machala, J. Tucek and R. Zboril, Polymorphous transformations of nanometric iron (III) oxide: a review, *Chem. Mater.*, 2011, **23**(14), 3255–3272.

42 R. M. Cornell and U. Schwertmann, *The Iron Oxides: Structure, Properties, Reactions, Occurrences and Uses*, John Wiley & Sons, 2003.

43 R. E. Vandenberghe, E. Van San, E. De Grave and G. M. Da Costa, About the Morin transition in hematite in relation with particle size and aluminium substitution, *Czech J. Phys.*, 2001, **51**(7), 663–675.

44 N. Popov, S. Krehula, M. Ristić, E. Kuzmann, Z. Homonnay, M. Bošković, D. Stanković, S. Kubuki and S. Musić, Influence of Cr doping on the structural, magnetic, optical and photocatalytic properties of α-Fe2O3 nanorods, *J. Phys. Chem. Solid.*, 2021, **148**, 109699.

45 R. Zboril, M. Mashlan, D. Krausova and P. Pikal, Cubic β-Fe2O3 as the product of the thermal decomposition of Fe2 (SO4) 3, *Hyperfine Interact.*, 1999, **120**(1), 497–501.

46 T. Danno, D. Nakatsuka, Y. Kusano, H. Asaoka, M. Nakanishi, T. Fujii, Y. Ikeda and J. Takada, Crystal

structure of β-Fe2O3 and topotactic phase transformation to α-Fe2O3, *Cryst. Growth Des.*, 2013, **13**(2), 770–774.

47 C. W. Lee, S. S. Jung and J. S. Lee, Phase transformation of β-Fe2O3 hollow nanoparticles, *Mater. Lett.*, 2008, **62**(4–5), 561–563.

48 T. P. Nguyen, Polymer-based nanocomposites for organic optoelectronic devices. A review, *Surf. Coat. Technol.*, 2011, **206**(4), 742–752.

49 E. Taboada, M. Gich and A. Roig, Nanospheres of silica with an ε-Fe2O3 single crystal nucleus, *ACS Nano*, 2009, **3**(11), 3377–3382.

50 J. Xue, Z. Zhou and J. Wang, Nanocrystalline Maghemite (γ-Fe2O3) in Silica by Mechanical Activation of Precursors, *J. Am. Ceram. Soc.*, 2002, **85**(4), 807–811.

51 M. Popovici, M. Gich, D. Nižňanský, A. Roig, C. Savii, L. Casas, E. Molins, K. Zaveta, C. Enache, J. Sort and S. De Brion, Optimized synthesis of the elusive ε-Fe2O3 phase *via* sol–gel chemistry, *Chem. Mater.*, 2004, **16**(25), 5542–5548.

52 J. Ma and K. Chen, Silica-free hydrothermal synthesis of ε-Fe2O3 nanoparticles and their oriented attachment to nanoflakes with unique magnetism evolution, *Ceram. Int.*, 2018, **44**(16), 19338–19344.

53 A. B. Abou Hammad, A. A. Al-Esnawy, A. M. Mansour and A. M. El Nahrawy, Synthesis and characterization of chitosan-corn starch-SiO2/silver eco-nanocomposites: Exploring optoelectronic and antibacterial potential, *Int. J. Biol. Macromol.*, 2023, **249**, 126077.

54 J. M. Xue, Z. H. Zhou and J. Wang, Synthesis of nanocrystalline γ-Fe2O3 in silica matrix by mechanical crystallization from precursor at room temperature, *Mater. Chem. Phys.*, 2002, **75**(1–3), 81–85.

55 F. Y. Alzoubi, O. Abu Noqta, T. Al Zoubi, H. M. Al-Khateeb, M. K. Alqadi, A. Abuelsamen and G. N. Makhadmeh, A novel one-pot synthesis of PVP-coated iron oxide nanoparticles as biocompatible contrast agents for enhanced T2-weighted MRI, *J. Compos. Sci.*, 2023, **7**(3), 131.

56 A. Davidson, E. Delahaye, V. Escax, N. El Hassan, R. Aquino, V. Dupuis, R. Perzynski and Y. Raikher, "Nanocasting": using SBA-15 silicas as hard templates to obtain monodispersed superparamagnetic gamma-Fe2O3 nanoparticles, *J. Phys. Chem. B*, 2006, **110**, 26001.

57 K. C. Barick, B. C. Varaprasad and D. Bahadur, Structural and magnetic properties of γ-and ε-Fe2O3 nanoparticles dispersed in silica matrix, *J. Non-Cryst. Solids*, 2010, **356**(3), 153–159.

58 I. Khan, S. Morishita, R. Higashinaka, T. D. Matsuda, Y. Aoki, E. Kuzmann, Z. Homonnay, S. Katalin, L. Pavić and S. Kubuki, Synthesis, characterization and magnetic properties of ε-Fe2O3 nanoparticles prepared by sol-gel method, *J. Magn. Magn Mater.*, 2021, **538**, 168264.

59 A. M. El Nahrawy, A. Elzwawy, A. B. Abou Hammad and A. M. Mansour, Influence of NiO on structural, optical, and magnetic properties of Al2O3–P2O5–Na2O magnetic porous nanocomposites nucleated by SiO2, *Solid State Sci.*, 2020, **108**, 106454.

60 M. Tadić, V. Spasojević, V. Kusigerski, D. Marković and M. Remškar, Formation of ε-Fe2O3 phase by the heat treatment of α-Fe2O3/SiO2 nanocomposite, *Scr. Mater.*, 2008, **58**(8), 703–706.

61 P. Brázda, J. Kohout, P. Bezdicka and T. Kmjec, α-Fe2O3 *versus* β-Fe2O3: Controlling the Phase of the Transformation Product of ε-Fe2O3 in the Fe2O3/SiO2 System, *Cryst. Growth Des.*, 2014, **14**(3), 1039–1046.

62 M. F. Silva, L. A. De Oliveira, M. A. Ciciliati, M. K. Lima, F. F. Ivashita, D. M. Fernandes de Oliveira, A. A. Hechenleitner and E. A. Pineda, The effects and role of polyvinylpyrrolidone on the size and phase composition of iron oxide nanoparticles prepared by a modified sol-gel method, *J. Nanomater.*, 2017, **2017**(1), 7939727.

63 V. J. Angadi, S. Kubrin, M. A. Sayed, A. Kumar, K. Sharma, M. Shkir, S. O. Manjunatha, R. A. Ribeiro, M. C. Oliveira, E. Longo and N. Basavegowda, Structural and magnetic modulations in α-Fe2O3 ceramic nanoparticles: A multifaceted study with DFT calculations, *Ceram. Int.*, 2025, **51**(21), 33407–33414.

64 E. Gorbachev, M. Soshnikov, M. Wu, L. Alyabyeva, D. Myakishev, E. Kozlyakova, V. Lebedev, E. Anokhin, B. Gorshunov, O. Brylev and P. Kazin, Tuning the particle size, natural ferromagnetic resonance frequency and magnetic properties of ε-Fe 2 O 3 nanoparticles prepared by a rapid sol–gel method, *J. Mater. Chem. C*, 2021, **9**(19), 6173–6179.

65 A. Elzwawy, A. M. Mansour, H. S. Magar, A. B. Abou Hammad, R. Y. Hassan and A. M. El Nahrawy, Exploring the structural and electrochemical sensing of wide bandgap calcium phosphate/CuxFe3-xO4 core-shell nanoceramics for H2O2 detection, *Mater. Today Commun.*, 2022, **33**, 104574.